Intracortical Microcirculatory Change Induced by Anesthesia in Rat Somatosensory Cortex

Kazuto Masamoto, Takayuki Obata, and Iwao Kanno

Abstract The present study aimed to characterize microcirculatory responses to anesthesia in brain tissue. With multi-photon excitation fluorescence microscopy, intra-cortical capillary dimension and red blood cell (RBC) flow were successfully visualized up to a depth of ~0.6 mm from the cortical surface in rats anesthetized with either isoflurane or α-chloralose. We observed that the diameter of the major cerebral artery was ~100 μm under isoflurane, but ~75 μm under α-chloralose. The capillary diameter was observed to be larger under α-chloralose than isoflurane: 5.1 ± 1.2 μm vs. 4.8 ± 1.1 μm, respectively. A significant difference in the mean RBC speed measured in single capillaries was observed: 0.4 ± 0.4 mm/s under α-chloralose vs. 1.5 ± 0.4 mm/s under isoflurane. In agreement with these observations, arterio-venous transit-time and laser-Doppler flowmetry consistently showed a significant reduction of the RBC and plasma blood speed under α-chloralose relative to isoflurane. These findings may indicate that local blood flow regulatory mechanisms exist at the capillary level for the balance of oxygen supply and demand induced by anesthesia in the brain tissue.

1 Introduction

A variety of brain tissue oxygen levels have been observed in animals under general anesthesia [1]. The direct and indirect effects of anesthesia involve the degree of anesthetic action on cerebral metabolic rate of oxygen (CMR_{O2}) and cerebral blood flow (CBF).

In a previous study, we found that rodents treated with inhalation anesthetics (e.g., isoflurane) or intravenous anesthetics (e.g., α-chloralose) that are widely used for brain activation studies, showed quite different behaviors for

K. Masamoto (✉)
Molecular Imaging Center, National Institute of Radiological Sciences, Chiba, 263-8555, Japan
e-mail: masamoto@nirs.go.jp

E. Takahashi, D.F. Bruley (eds.), *Oxygen Transport to Tissue XXXI*, Advances in Experimental Medicine and Biology 662,
DOI 10.1007/978-1-4419-1241-1_7,

the activation-induced cortical hemodynamics [2]. Since hemodynamic-based brain imaging techniques rely on the microcirculatory responses to local neural activity, the effects of anesthesia on the brain microcirculation are critically important for interpretation of the imaging signals. However, the effects of anesthesia on the brain microcirculation, such as vessel dimension and red blood cell (RBC) flow remain unaddressed.

In the present study, we directly measured intracortical capillary dimension and RBC flow in the cerebral cortex of rats anesthetized with either volatile isoflurane or injectable α-chloralose. A biocompatible fluorescent dye was intravenously injected for visualization of blood plasma and cortical microvasculature was three-dimensionally visualized with in vivo multi-photon excitation fluorescent microscopy up to a depth of 0.6 mm from the cortical surface. Intraluminal vascular dimension and fluorescently labeled RBC speed were then measured.

2 Materials and Methods

All animal protocols were approved by the NIRS Animal Experiment Committee. The animals (250–350 g Sprague-Dawley rats, $N=9$) were initially anesthetized with 4–5% isoflurane and maintained with 2% during surgical procedures. The animal was mechanically ventilated and physiologic parameters (e.g., end-tidal CO_2, anesthetic gas concentration, respiratory rate, heart rate, and mean arterial blood pressure) were monitored throughout all experiments. Arterial blood gas was periodically measured, and respiratory rate and minute ventilation volume were adjusted as needed. Rectal temperature was maintained at 37.0 ± 0.2°C.

A portion of the left skull (3 mm by 3 mm) over the somatosensory area was removed. The opened area was filled with physiologic saline solution. For experiments, the anesthesia level was first maintained with isoflurane (~1.4%) and then switched to α-chloralose (45 mg/kg/h, i.v.), as previously reported [2]. For visualization of the cortical vasculature, a bolus of Qdot® 605 (1 μM in buffered solution, Invitrogen) was intravenously injected (0.2–0.4 ml). The cortical vasculature was then visualized with multi-photon excitation fluorescent microscope (TCS SP5, Leica Microsystems) with an excitation wavelength of 900 nm (Mai-Tai, Ti:Sapphire laser, Spectra-Physics). The objective lens was a 20× water-immersion lens (0.5 NA, Leica Microsystems). The 512 pixel by 512 pixel images covered a cortical area of 456 μm by 456 μm with a pixel resolution of 0.89 μm. To obtain the three-dimensional structure, contiguous images were captured up to a depth of 0.6 mm from the cortical surface with a step size of 0.01 mm in the z-direction. The region of interest was selected with care to avoid areas having vessels of a relatively large size at the cortical surface. A final image was taken to cover an area of 912 μm by 912 μm in the x-y plane by scanning four adjacent regions. For display purposes, a maximum-intensity projection was constructed from contiguous images obtained in the z-direction.

Based on their pulsation and branching geometry, arterial and venous networks were distinguished at the cortical surface, and then tracked into the parenchyma tissue. To measure capillary diameter, a maximum intensity projection was created from every 0.1-mm thickness in the z-direction and then the width in the image was calculated. A single capillary was defined as the single vessel having cross-sectional thickness less than 8 μm and for which both edges continued to two new vessels as a branching.

The RBC speed was measured by tracking a FITC-labeled RBC through a single capillary. Time-lapse images were obtained at a rate of 14–167 frames per second, depending on the number of lines to be scanned in each single frame. The scanning area was set to cover the whole structure of the single-capillary shape (i.e., 64–256 lines). Similarly, the speed of blood plasma was evaluated by tracking 0.1-μm diameter fluorescent beads that were intravenously injected. For the measurement of mean arterio-venous transit time, a bolus injection (0.1 ml) of fluorescently labeled RBCs or fluorescent beads was performed via the femoral vein. The time-lapse image was obtained with a 5× objective lens at a rate of seven frames per second. Statistical significance was determined with a *t*-test ($P < 0.05$).

3. Results

There was no detectable difference in the measured physiologic parameters (arterial blood gas and blood pressure) between isoflurane and α-chloralose conditions (Table 1). We observed that the diameter of the principal artery at the cortical surface was ~100 μm under isoflurane, but ~75 μm under α-chloralose. The results showed that the principal artery shrank significantly after induction with α-chloralose. However, the intracortical capillary diameter was slightly larger under α-chloralose (5.1 ± 1.2 μm, $n = 1682$ vessels) compared to the isoflurane condition (4.8 ± 1.1 μm, $n = 1746$ vessels). A statistically significant difference was observed between two conditions. These results indicate that the upstream and downstream vessels react differently depending on the anesthetics.

Table 1 Blood gas conditions, mean arterial blood pressure (BP), and mean capillary diameter (Dc) observed under isoflurane (Iso) and α-chloralose (Acl) conditions (Mean ± SD, $N = 9$). *$P < 0.05$ (Iso vs. Acl)

	*p*H	pCO_2 (mmHg)	pO_2 (mmHg)	BP (mmHg)	Dc (μm)
Iso	7.43 ± 0.03	37 ± 3	128 ± 18	94 ± 11	4.8 ± 1.1
Acl	7.44 ± 0.02	36 ± 2	123 ± 16	115 ± 15	5.1 ± 1.2*

The mean RBC speed in a single capillary was significantly lower under α-chloralose relative to the isoflurane condition: 0.4 ± 0.4 mm/s under α-chloralose vs. 1.5 ± 0.4 mm/s under isoflurane. Under α-chloralose, some RBCs were found

to be very slow (<0.01 mm/s), whereas most RBCs measured under isoflurane had a relatively high speed (0.4–3.0 mm/s).

As expected, the arterio-venous transit-time of the labeled RBCs was significantly longer under α-chloralose (2.8 ± 1.7 s at peak-to-peak) as compared to the isoflurane condition (1.0 ± 0.9 s). Similar results were observed for the transit time of blood plasma: 1.8 ± 1.3 s under α-chloralose and 1.2 ± 0.7 s under isoflurane. These results indicated that the both RBC and plasma blood speed were significantly lower under α-chloralose relative to isoflurane conditions.

4 Discussion

It has been previously shown by other groups that the baseline CBF under α-chloralose was 30–50% lower than under isoflurane in rat somatosensory cortex, i.e. 70–90 mL/100 g/min under α-chloralose [3, 4] vs. 130–150 mL/100 g/min under isoflurane [5, 6]. In a previous study, we found the baseline CBF measured with laser-Doppler flowmetry was 31% lower under α-chloralose compared with isoflurane [2]. Our measurements of the arterial dimension are in good agreement with these literature data, indicating that the tone in the upstream resistance vessels has a significant role in the regulatory mechanism of the baseline CBF induced by anesthesia. However, we also found that the effect of the anesthesia on the intracortical capillary diameter was opposite to the arterial response. Namely, a larger capillary diameter was observed under α-chloralose as compared to the isoflurane condition. This might indicate that the upstream arteries and intracortical microvessels have separate or independent mechanisms for the regulation of local CBF.

Our results for the mean RBC speed consistently showed that the speed was significantly lower under α-chloralose relative to the isoflurane condition. The results are consistent with previous CBF data. However, the measured RBC speed under isoflurane was relatively high. Kleinfeld et al. (1998) reported that the intra-cortical RBC speed was 0.77 mm/s in rats anesthetized with urethane [7]. The ranges of RBC speed in capillaries were reported as 0.3–3.2 mm/s [8]. In the present study, we showed that the variable speed of RBCs could be due to a local regulatory mechanism rather than upstream arterial regulation. Since the capillary volume and speed of RBCs critically affect oxygen transfer processes from nearby blood vessels to the energy consuming tissue site, it is worthwhile to compare the tissue oxygen level between both anesthesia conditions. Our group has reported that the mean tissue oxygen level in rat somatosensory cortex was 29 mmHg under α-chloralose and 33 mmHg under isoflurane [9, 10]. Another study with electron paramagnetic resonance oximetry showed that the mean tissue oxygen level at normoxic conditions was 13 mmHg under a cocktail of α-chloralose and urethane and 38 mmHg under isoflurane [11]. The data from those studies were in good agreement with the CBF data; higher CBF produces higher tissue oxygen and vice versa. The anesthesia may also affect the tissue oxygen metabolic rate in a different manner, and thus a possible scenario

where the effect of anesthesia on the energy metabolism becomes a dominant factor leading to the observed difference in tissue oxygen level cannot be ruled out. However, it should be noted that endothelial cells have the ability to control their dimension by sensing the nearby blood oxygenation level [12], which may play a role in adjusting local oxygen demand and supply via regulation of capillary volume and RBC speed. Further studies are needed to elucidate the full regulatory mechanism for the local regulation of the microvascular dimensions and RBC traffic.

Acknowledgments This work was partially supported by KAKENHI (#19800065).

References

1. Ndubuizu, O., LaManna, J. C., 2007, Brain tissue oxygen concentration measurements, Antioxid Redox Signal. 9:1207–1219.
2. Masamoto, K., Kim, T., Fukuda, M., Wang, P., Kim, S. G., 2007, Relationship between neural, vascular, and BOLD signals in isoflurane-anesthetized rat somatosensory cortex, Cereb Cortex. 17:942–950.
3. Ueki, M., Linn, F., Hossmann, K. A., 1988, Functional activation of cerebral blood flow and metabolism before and after global ischemia of rat brain, J Cereb Blood Flow Metab. 8:486–494.
4. Lee, S. P., Duong, T. Q., Yang, G., Iadecola, C., Kim, S. G., 2001, Relative changes of cerebral arterial and venous blood volumes during increased cerebral blood flow: implications for BOLD fMRI, Magn Reson Med. 45:791–800.
5. Maekawa, T., Tommasino, C., Shapiro, H. M., Keifer-Goodman, J., Kohlenberger, R. W., 1986, Local cerebral blood flow and glucose utilization during isoflurane anesthesia in the rat, Anesthesiology. 65:144–151.
6. Lenz, C., Frietsch, T., Futterer, C., Rebel, A., van Ackern, K., Kuschinsky, W., Waschke, K. F., 1999, Local coupling of cerebral blood flow to cerebral glucose metabolism during inhalational anesthesia in rats: desflurane versus isoflurane, Anesthesiology. 91:1720–1723.
7. Kleinfeld, D., Mitra, P. P., Helmchen, F., Denk, W., 1998, Fluctuations and stimulus-induced changes in blood flow observed in individual capillaries in layers 2 through 4 of rat neocortex, Proc Natl Acad Sci U S A. 95:15741–15746.
8. Hudetz, A. G., 1997, Blood flow in the cerebral capillary network: a review emphasizing observations with intravital microscopy, Microcirculation. 4:233–252.
9. Masamoto, K., Kershaw, J., Ureshi, M., Takizawa, N., Kobayashi, H., Tanishita, K., Kanno, I., 2007, Apparent diffusion time of oxygen from blood to tissue in rat cerebral cortex: implication for tissue oxygen dynamics during brain functions, J Appl Physiol. 103:1352–1358.
10. Masamoto, K., Vazquez, A., Wang, P., Kim, S. G., 2008, Trial-by-trial relationship between neural activity, oxygen consumption, and blood flow responses, Neuroimage. 40:442–450.
11. Hou, H., Grinberg, O. Y., Taie, S., Leichtweis, S., Miyake, M., Grinberg, S., Xie, H., Csete, M., Swartz, H. M., 2003, Electron paramagnetic resonance assessment of brain tissue oxygen tension in anesthetized rats, Anesth Analg. 96:1467–1472.
12. Inoue, K., Tomita, M., Fukuuchi, Y., Tanahashi, N., Kobari, M., Takao, M., Takeda, H., Yokoyama, M., 2003, Dynamic observation of oxygenation-induced contraction of and transient fiber-network formation-disassembly in cultured human brain microvascular endothelial cells, J Cereb Blood Flow Metab. 23:821–828.

Ann Nucl Med (2010) 24:1–11
DOI 10.1007/s12149-009-0323-8

ORIGINAL ARTICLE

Development of motion correction technique for cardiac ^{15}O-water PET study using an optical motion tracking system

Kazuhiro Koshino · Hiroshi Watabe · Shinji Hasegawa · Takuya Hayashi · Jun Hatazawa · Hidehiro Iida

Received: 19 August 2009 / Accepted: 9 October 2009 / Published online: 3 December 2009

Abstract
Objective Cardiac ^{15}O-water PET studies provide an accurate quantitation of regional myocardial blood flow (rMBF). We developed a motion correction system using an optical motion-tracking device to detect a subject's global movement for cardiac study.
Methods PET studies were carried out on a cardiac phantom and a healthy volunteer at rest. The three-dimensional locations of the markers attached to the subjects during scans were measured using an optical motion-tracking system. In the phantom study, we performed a transmission scan and seven ^{18}F emission scans of a baseline and with artificial misalignment of shifts and rotations. The correlation coefficients between the baseline and the other images before and after the corrections for the misalignment were calculated. In the human study, we performed a ^{15}O-water dynamic scan with a transmission and axially 30 mm-shifted transmission scans. Motion of the subject was estimated by the information from the system, and was corrected on each sinogram using attenuation maps realigned to dynamic frames. Reconstructed dynamic images were then realigned to the transmission data. We calculated rMBF values for nine segments and myocardial images from the emission images, which were reconstructed with the first attenuation map (reference) and with the misaligned attenuation map before and after our corrections.
Results In the phantom study, the correlation coefficients were improved from 0.929 ± 0.022 to 0.987 ± 0.010 (mean ± SD) after the corrections. In the human study, the global and cyclic movements were detected. The cyclic movement due to respiration was smoothed by frame-averaging, and reasonable information of the global movement was obtained. The rMBF value (mean ± SD) was 0.94 ± 0.12 mL/min/g for the reference. The rMBF values using the misaligned attenuation map changed from 1.03 ± 0.21 to 0.93 ± 0.11 mL/min/g after the correction, and spurious defects in myocardial images were also recovered.
Conclusions Our technique provided reasonable information for correcting the global movement of the subject. It was shown that this system was applicable to detect and correct subject movement in cardiac PET studies at rest.

Keywords Myocardial blood flow · PET · Motion correction · Attenuation correction · ^{15}O-labeled water

K. Koshino (✉) · H. Watabe · H. Iida
Department of Investigative Radiology,
National Cardiovascular Center Research Institute,
5-7-1 Fujishirodai, Suita, Osaka 565-8565, Japan
e-mail: koshino@ri.ncvc.go.jp

S. Hasegawa
Department of Cardiology, Osaka Koseinenkin Hospital,
Osaka, Japan

T. Hayashi
Functional Probe Research Laboratory,
RIKEN Center for Molecular Imaging Science, Hyogo, Japan

J. Hatazawa
Department of Nuclear Medicine and Tracer Kinetics,
Osaka University Graduate School of Medicine, Osaka, Japan

Introduction

Motion of a patient during a positron emission tomography (PET) scan can cause deterioration in image quality and quantitative accuracy. Several techniques have been

proposed for motion compensation in neuroimaging [1–7]. In cardiac PET studies, effects of wall contractile and respiratory motion can be smoothed in the temporary sampled PET images, but global movement of the patients during the relatively long scanning period is still a significant source of errors [8–11].

It was shown that misalignment by a 20-mm shift in the lateral/septal direction between transmission and ^{18}F-fluorodeoxyglucose (^{18}FDG) emission scans caused a 30% change in regional activity in cardiac ^{18}F-FDG PET [8]. To align two ^{18}F-FDG emission images acquired on different days, Bacharach et al. [11] proposed a registration technique based on the rigid body model using the transmission images by assuming no misregistration between transmission and emission data sets.

Cardiac ^{15}O-water PET studies provide quantitative information with regard to the viabilities of myocardium using the myocardial blood flow (MBF), coronary flow reserve, and perfusable tissue index [12–19]. Naum et al. [20] demonstrated that the movement occurred during dynamic scans with cycling. They proposed a method to correct for the motion during a single dynamic scan, and among different sessions, by aligning the dynamic frames of ^{15}O-water images using two external radioactive markers placed on the back of a subject. Although their technique did not provide correction for misalignment between transmission and emission data, reasonable improvement in calculated MBF values was demonstrated.

Correcting the misalignment between the transmission and emission data is a challenging task because the image contrast of transmission images differs from that of emission images. The distribution of ^{15}O-water also varies dramatically in regions of the right and left ventricles, myocardium, and other organs over time. Additionally, the image quality of PET with ^{15}O-water is worse than that with other radioligands due to the short half life of ^{15}O, which makes image registration difficult.

In this paper, we describe a novel approach using an optical motion-tracking system for detecting the subject's global movement during the relatively long study period, as an extension of the early studies of Watabe et al. [4]. The proposed technique provided correction for misalignment between dynamic emission sinograms, and also provided accurate attenuation correction, in which misalignment between attenuation map and each emission sinogram was corrected in the reconstruction stage.

First, the inherent accuracy of our system was evaluated. Then, the system was validated on a cardiac phantom study for artificial misalignment between an attenuation map and emission data. Correction for global movement obtained by monitoring the locations of external markers on chest skin was validated in a ^{15}O-water cardiac PET study in a healthy volunteer at rest.

Materials and methods

Hardware-based position monitoring system

To detect motion of a subject, we adopted an optical motion-tracking device in which targets attached to the chest skin are monitored. The motion compensation approach using an optical motion-tracking system has been previously validated in brain PET studies [3–7]. We applied this approach to the cardiac PET studies. Figure 1a shows an optical motion-tracking system, POLARIS (Northern Digital Inc., Canada). The POLARIS has two charge-coupled-device cameras, and provides the 3D position of a target. The three-dimensional position is measured in the form of 6 degrees of freedom: three rotational angles, and three translational directions. The manufacturer reports that the accuracy of the rotational angle and translation are better than 0.3° and 0.5 mm, respectively. Figure 1b shows a target with four infrared-reflective markers and supporting post. The target and supporting post made of carbon resin were pinned with two fluoroplastic screws. Figure 1c shows the position calibration tool used to convert the locations of subject positions in the POLARIS coordinate into PET coordinates. Figure 1d represents the schematic diagram of our system. Locations of targets attached to the chest skin of the subject and the gantry of a PET scanner were measured with the POLARIS. The target on the gantry of the PET scanner was used as a reference in order to convert the subject's positions from the POLARIS coordinate to the PET coordinate. Figure 1e shows an example of the experimental setup with a healthy volunteer in the cardiac PET study. Two targets were attached to the chest skin of the subject. Three legs of the supporting post were attached to the skin of the subject using surgical tape. The axial field-of-view (FOV) of the PET scanner used in the human study, HEADTOME-V tomography (SHIMADZU Corp., Kyoto, Japan), was 200 mm, and the gantry diameter was 850 mm [21]. The geometries of targets attached to the thoracic surface were 85×85 mm^2 (the left-hand target in Fig. 1e, target 1) and 65×90 mm^2 (the right-hand target in the Fig. 1e). The heights of supporting posts for target 1 and target 2 were 50 and 42 mm, respectively. We calculated the subject's positions in the PET coordinate by measuring the locations of the target with four infrared-reflective markers (the primary target). Another target was used as a reserve in cases when the primary target was hidden from the FOV of the POLARIS.

Motion correction

The rigid motion correction technique employed is an extension of the previous work for brain PET studies by

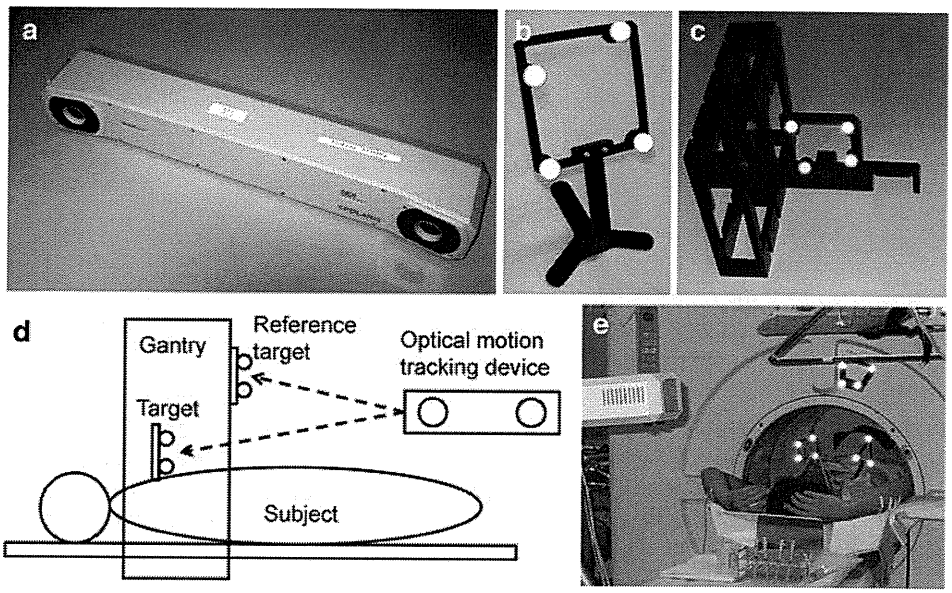

Fig. 1 Our motion correction system. **a** Optical motion-tracking device. **b** Target consists of infrared-reflective markers with supporting post. **c** Position calibration tool with a target. **d** Schematic diagram of the system. Locations of the targets on the subject and the gantry were measured with the optical motion-tracking device. **e** An example of the experimental configuration

Watabe et al. [4]. We consider four coordinates: the POLARIS C_S, a target on a PET gantry for reference C_G, a target attached on a subject C_T, and the PET scanner C_P. By measuring the location and orientation of each target attached to the subject and the gantry using the POLARIS, we obtained a 4 × 4 transformation matrixes, $T_{T\to S}$ from C_T to C_S, and $T_{G\to S}$ from C_G to C_S, respectively. Motion matrix $M_{P_1\to P_2}$ from a position $P_1 = P(t_1)$ to another position $P_2 = P(t_2)$ in the PET coordinate is written as follows [4]:

$$M_{P_1\to P_2} = T_{G\to P}T^{-1}_{G\to S}T_{T_1\to S}T^{-1}_{T_2\to S}T_{G\to S}T^{-1}_{G\to P} \quad (1)$$

where T_1 and T_2 are positions in target coordinates corresponding to positions P_1 and P_2 in the PET coordinate. $T_{G\to P}$ is the matrix to transform a position from the gantry coordinate to the PET coordinate. The matrix is given by the following equation:

$$T_{G\to P} = T_{S\to P}T_{G\to S} \quad (2)$$

$T_{S\to P}$ is the matrix which relates the POLARIS and PET coordinates and is obtained by position calibration.

The point source was embedded in a given position of a target, which is fixed on the calibration tool shown in Fig. 1c. By measuring the position of the point source using the POLARIS, the position $P_S = (x_S, y_S, z_S)$ of the point source in the POLARIS coordinate is calculated using the known position $P_T = (x_T, y_T, z_T)$ in the target coordinate and $T_{T\to S}$, as $P_S = T_{T\to S}P_T$. The position $P_P = (x_P, y_P, z_P)$ in the PET coordinate is also obtained from the reconstructed emission image. By changing the position of the target, in which the point source is embedded, $T_{S\to P}$ is calculated using the least-squared-fit between the pairs of P_Ss and P_Ps. The PET coordinate was

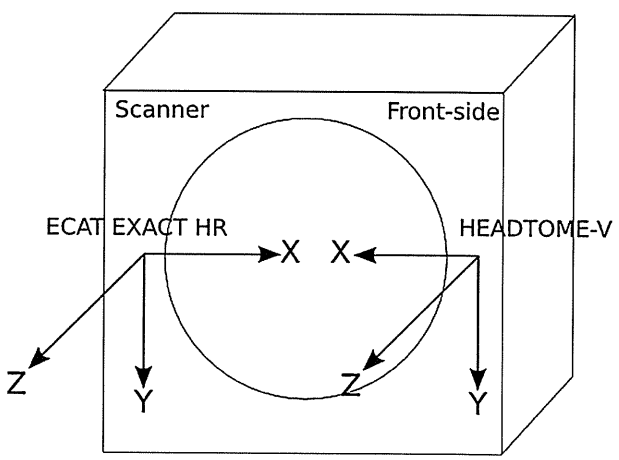

Fig. 2 PET coordinates defined by position calibrations

defined by the position calibration as shown in Fig. 2. The positions of subjects in the PET coordinate will be discussed in the following.

To correct a subject's movements during a dynamic acquisition of an emission scan with multiple frames, we estimated the heart locations from the locations of the target, which are measured by the POLARIS. The displacement of the COG of the heart's position from during the transmission scan to during each dynamic frame of the emission scan is given by

$$\begin{aligned} H^F - H^{TCT} &= \frac{1}{L}\sum_t^F H(t) - \frac{1}{N}\sum_t^{TCT} H(t) \\ &= \frac{1}{L}\sum_t^F [P(t) + \Delta(t)] - \frac{1}{N}\sum_t^{TCT} [P(t) + \Delta(t)] \end{aligned} \quad (3)$$

where H^{TCT} and H^{F} are the averaged COGs of the heart positions during the transmission and the dynamic frame, $H(t)$ and $P(t)$ are the COGs of positions of the heart and the target at time t, $\Delta(t)$ is a term representing a non-rigid relation for positions at time t between the heart and the target, L and N are the numbers of measurements of the target's positions by the POLARIS during acquisition of the dynamic frame and the transmission scan, respectively. For motion correction, we assumed the rigid body model, in which the target and the COG of the heart's position have linear movement at least in the FOV of a PET scanner, that is, we assumed that summations of $\Delta(t)$ for the transmission scan and the dynamic frame equal to zero. The procedures of our motion-correction technique are as follows: (1) An attenuation map is aligned to the coordinate of a dynamic frame of an emission scan using the motion matrix in Eq. 1, in which P_1 and P_2 are $\Sigma^{TCT}P(t)/N$ and $\Sigma^{F}P(t)/L$ in Eq. 3. (2) The attenuation map is then converted to its sinogram by forward projection. (3) Each sinogram of the dynamic frames is reconstructed with the realigned attenuation sinogram. (4) The emission image is aligned to the transmission coordinate with the inverse matrix of the motion matrix. (5) Last, procedures from 1 through 4 are repeated for all dynamic frames of the emission data.

Position calibrations

Position calibrations were performed on two PET scanners to obtain a matrix $T_{G\to P}$ in Eq. 2, which transforms the subject's positions from a gantry coordinate to a PET coordinate. For ECAT EXACT HR tomography (CTI/Siemens, Knoxville, TN, USA) [22] used in a cardiac phantom study, ten emission scans were performed, each displaying different positions of a radioactivity point source of ^{18}F solution, using the calibration tool in Fig. 1b. For the PET scanner used in a healthy volunteer study, 14 emission scans were performed with the ^{18}F solution point source and calibration tool.

The accuracy of the calibrations was evaluated from $T_{G\to S}$ and $T_{S\to P}$ in Eq. 2. The accuracy of $T_{G\to S}$ part was evaluated by determining the standard deviation (SD) of rotational angles and translations calculated from position data of the gantry, because $T_{G\to S}$ depends on only the accuracy of the measurements in regard to the POLARIS. To evaluate the accuracy of $T_{S\to P}$ part, we calculated errors between a position of a point source P_P, and the approximation position using $T_{S\to P}$, $P_X = T_{S\to P}P_S$:

$$e(i,k) = P_X(i,k) - P_P(i,k) \tag{4}$$

$$\mathrm{RMSE}(i) = \sqrt{\sum_{k=x,y,z} |P_X(i,k) - P_P(i,k)|^2} \quad (k = X,Y,Z \text{ and } i = 1,\ldots,N) \tag{5}$$

where $e(i, k)$ is the approximation error of a point source in the ith position for each direction, X, Y, and Z are orthogonal axes in Fig. 2, RMSE(i) is the root mean square error, and N is the number of positions of a point source.

Phantom study

To validate our correction technique for the misregistration between the attenuation map and emission data, we performed PET scans using a cardiac phantom (KYOTO KAGAKU co., LTD, Kyoto, Japan, type HL-D) and the ECAT EXACT HR tomography. The phantom mimics the human thoracic region and has cardiac and liver inserts. The insert can be filled with radioisotope solution. The myocardium and liver inserts were filled with the ^{18}F solution of relative activities of 1 and 4. A target (without the supporting port) for the POLARIS was attached to the phantom using polyethylene cross tape. Then, we performed a 1,000-s transmission scan for attenuation corrections. After the transmission scan, seven ^{18}F emission scans were performed with a set of single frame data for 180 s. The first scan was the baseline (scan #1), in which there was no misalignment to the transmission. For the following three emission scans (scan #2–4), the phantom was moved in the X, Y, and Z directions. For the other three scans, the phantom was rotated about the X, Y, and Z axes (scan #5–7). The phantom's positions were measured with the POLARIS.

The reconstructed images before and after the correction were obtained using an FBP (filtered back-projection) algorithm with a Gaussian filter of 6 mm FWHM (full-width at half-maximum). The matrix size and voxel size of images were 128 × 128 × 47 and 4.4 × 4.4 × 3.1 mm^3, respectively. All emission data were corrected for physical decay of ^{18}F with base time as the start of the first emission scan, and all of the emission images were reoriented to the short axis using a transformation matrix.

To evaluate the effects of the corrections, we calculated correlation coefficients for myocardial regions between the baseline and misaligned emission images, both before and after the corrections.

Human study

A cardiac ^{15}O-water PET study was performed on a healthy volunteer (male, 32 years old) using the HEADTOME-V tomography in order to validate use of the external markers on the chest skin and also to evaluate the effects of the global movement on the quantification of MBF by artificial misalignment between attenuation and emission data. The healthy volunteer gave written informed consent according to a protocol approved by the Ethical Committee and

Internal Review Board of Osaka University. The PET study consisted of a 20-min transmission scan, an 8-min ^{15}O-CO emission scan for blood pool imaging, a 6-min ^{15}O-water emission scan with 26 dynamic frames (12 × 5, 8 × 15 and 6 × 30 s), and a second 20-min transmission scan. All scans were acquired in a 2D acquisition mode. The radioactivity of inhaled ^{15}O-CO gas was 3.2 GBq. ^{15}O-water was injected via the left brachial vein; activity was 1.1 GBq for 40 s. All scans were performed without pharmacological stress. To investigate the accuracy of the POLARIS for tracking the locations of the target attached to the thorax skin of the subject, the couch of the PET scanner was moved +30 mm along the axial direction before the second transmission scan, corresponding to the Z direction in Fig. 2, with the subject lying on the couch. It was expected that the shift in the $+Z$ direction caused the artificial deterioration of image quality and quantitative accuracy in especially the anterior and lateral regions. The subject's positions during the scans were monitored by the POLARIS, at a frequency of one sample per second.

The reconstructed images for the four cases were obtained using an FBP algorithm with a Gaussian filter of 9 mm FWHM. The matrix and voxel sizes of the reconstructed images were 128 × 128 × 63 and 2.03 × 2.03 × 3.13 mm^3. No scatter correction was performed during the image reconstruction stage.

Regional MBF values were estimated for four cases. Case 1: the first attenuation map and emission data, case 2: the first attenuation map and emission data with correction for the subject's motions, case 3: the second attenuation map and the emission data, case 4: the second attenuation map and the emission data after the correction for the subject's motions and the 30-mm-shifted misalignment. Differences in the MBF values for cases 1 and 2 were considered to indicate effects from the correction for the frame-averaged motion if the subject's motion was small. Differences in MBF values for cases 1 and 3 could indicate errors in the quantification of MBF caused by the artificial misalignment between the second attenuation map and the emission data. The lack of any difference in MBF values for cases 1 and 4 indicated that our technique tracked the shift of the target on the thorax skin accurately and corrected the misalignment. In order to generate cases 2 and 4, the positions P_1 and $P_2^{(j)}$ in Eq. 1 were calculated as averaged COGs of the subject's positions during the first and second transmission scans and the jth dynamic frame of ^{15}O-water or C^{15}O emission scan. Using Eq. 1 with P_1 and $\{P_2^{(j)}\}$, we performed frame-by-frame motion corrections for all dynamic frames of emission data. Due to the fact that the PET scanner did not provide a dynamic transmission scan, we assumed that the subject did not move during the transmission scan.

For quantification of MBF, we employed a compartment analysis model proposed by Iida et al. [13], which provided corrections for spillover from a left ventricle and partial volume effect and generated a MBF value in units of mL/min/g of perfusable tissue. All transmission and emission images were reoriented to the short axis. To calculate tissue time activity curves, regions of interest (ROIs) were drawn in nine myocardial regions: apical, mid-anterior, mid-lateral, mid-posterior, mid-septal, basal-anterior, basal-lateral, basal-posterior, and basal-septal regions. To avoid spillover effects from the right ventricle, the sizes of ROIs in septal regions were smaller than those in other regions. Another ROI was drawn on the left ventricle in order to estimate the arterial input function [19]. These ROIs were manually and independently drawn for the four cases. In addition, to validate the consistency between the quantitative results of MBF values and the quality of the images, we calculated the build-up and washout phase images [23] for the four cases. The build-up and washout phase images were obtained by subtracting a blood pool image from summed images of early (0–180 s) and later (180–360 s) frames of a ^{15}O-water image.

We evaluated the magnitude of the subject's motions in the PET coordinate during each scan. We defined position P_1 in Eq. 1 as the position at the start of the first transmission scan, and position P_2 as the position at an arbitrary time during a transmission or an emission scans. The rotational angles and translations for arbitrary times were obtained using Eq. 1. We represented motion during a scan in the form of mean ± SD for each rotational angle and translation.

Results

Position calibrations

Table 1 shows the inherent accuracy of our system in the two PET scanners. Values of SDs for rotations and translations obtained from $T_{G\to S}$ data were very small. Table 1 also shows the approximation errors (mean ± SD) occurred while transforming the positions of a point source from the POLARIS coordinate to the PET coordinate using $T_{S\to P}$. There was no bias in any direction in either scanner. Each value of RMSE was smaller than the spatial resolution of the corresponding scanner [21, 22].

Cardiac phantom study

Table 2 lists the observed misalignment from the reference position of the phantom in the transmission scan and the correlation coefficients between the reference image and the misaligned images before and after the corrections (mean ± SD; 0.929 ± 0.022 and 0.987 ± 0.010). The

Table 1 Inherent accuracy of the motion correction system in the two PET scanners

Scanner	$T_{G\to S}$						$T_{S\to P}$				# of point positions
	Rotational angle (deg)			Translation (mm)			e_x	e_y	e_z	RMSE	
	r_x	r_y	r_z	t_x	t_y	t_z					
ECAT EXACT HR	0.0	0.0	0.0	0.0	0.0	0.0	0.0 ± 0.8	0.0 ± 0.9	0.0 ± 0.8	1.3 ± 0.4	10
HEADTOME-V	0.0	0.0	0.0	0.0	0.0	0.1	0.0 ± 1.5	0.0 ± 1.6	0.0 ± 0.6	2.3 ± 0.2	14

Standard deviations of rotational angles and translations obtained from $T_{G\to S}$ data and approximation errors (mean ± SD in mm) by transforming positions of a point source from the POLARIS coordinate to the PET coordinate using $T_{S\to P}$. Columns $T_{G\to S}$, r_x, r_y and r_z denote SDs of rotational angles about three orthogonal *X*, *Y*, and *Z* axes, respectively. t_x, t_y and t_z denote SDs of translations along three orthogonal axes, respectively. Columns $T_{S\to P}$, e_x, e_y, and e_z denote average values (mean ± SD in mm) of $e(i, X)$, $e(i, Y)$, and $e(i, Z)$, respectively. $e(i, k)$ was defined in Eq. 4. *RMSE* denotes an average value (mean ± SD in mm) of *RMSE*(*i*), defined in Eq. 5

Table 2 The observed misalignment and correlation coefficients for the phantom study

Scan no.	Rotation (deg)			Translation (mm)			Correlation coefficient	
	r_x	r_y	r_z	t_x	t_y	t_z	Before MC	After MC
2	0.0	0.2	5.1	35.7	0.8	−3.4	0.896	0.997
3	0.0	−1.0	1.3	0.9	35.2	3.2	0.938	0.995
4	0.0	−0.2	0.9	5.9	0.1	42.8	0.917	0.971
5	13.1	1.4	0.4	1.9	22.5	17.1	0.926	0.986
6	2.4	−15.6	−2.1	10.9	3.8	4.7	0.938	0.982
7	−0.6	1.8	−13.5	13.4	11.9	−9.5	0.960	0.992

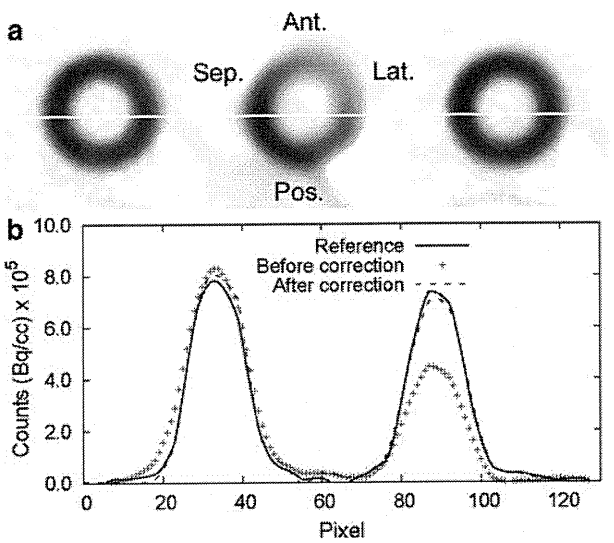

Fig. 3 Reconstructed and reoriented images of the phantom. **a** Reconstructed images. *Left*, *mid*, and *right* columns represent the reference emission image (no misalignment), the second emission images before correction for misalignment, and the second emission images after correction for the misalignment, respectively. **b** Profiles at the level of white lines in images. *Solid line*, *cross symbols*, and *dashed lines* represent the first emission image, the second emission images before correction, and the second emission images after correction, respectively

effects of our correction technique are demonstrated in Fig. 3. The left column in Fig. 3a is the reference emission image (no misalignment). The middle and right columns represent the emission images with the misalignment of the *X*-direction before and after the corrections. For the image in the middle column, only the position was transformed to the transmission coordinate after the reconstruction. Figure 3b represents line profiles at the level of white lines in the slices.

Human study

Table 3 summarizes the observed movements of the subject during scans relative to the beginning of the first transmission scan, in the form of rotational angles about and translations along three orthogonal axes. It was observed that the magnitude of the average parts of the rotational angles and translations tended to increase. The value of t_z changed from -1.8 ± 0.6 to 28.3 ± 0.6 mm between the ^{15}O-water emission and the second transmission scan mainly because of the 30-mm shift of the couch as well as the motions of the subject. There was little change in the SD in any rotational angle or translation among the scans.

Figure 4 shows motion parameters during ^{15}O-water scan. Figure 4a and b represent the sample-by-sample and frame-averaged translations. Figure 4c and d shows the sample-by-sample and frame-averaged rotational angles.

Table 4 shows that the MBF values (mean ± SD), which were obtained from nine myocardial segments, were 0.94 ± 0.12, 0.91 ± 0.13, 1.03 ± 0.21, and 0.93 ± 0.11 mL/min/g for the four cases. The values for cases 1 and 2 were obtained from the emission data and the first attenuation map before and after motion correction. The values for cases 3 and 4 were obtained from the emission data and the second attenuation map before and after the corrections for the subject's motions and the 30-mm shift of the couch. There were significant

Table 3 Observed movements (mean ± SD) of the healthy volunteer during scans relative to the beginning of the first transmission scan

Scan	Rotational angle (deg)			Translation (mm)		
	r_x	r_y	r_z	t_x	t_y	t_z
TCT 1	−0.1 ± 0.2	−0.4 ± 0.2	−0.2 ± 0.2	0.7 ± 0.5	1.3 ± 0.6	1.0 ± 0.8
$C^{15}O$	0.0 ± 0.2	−0.1 ± 0.2	−0.7 ± 0.1	2.6 ± 0.3	1.0 ± 0.5	−1.7 ± 0.7
^{15}O-water	0.4 ± 0.2	0.0 ± 0.1	−0.7 ± 0.1	2.7 ± 0.2	1.3 ± 0.4	−1.8 ± 0.6
TCT 2	−0.4 ± 0.2	0.7 ± 0.2	−2.0 ± 0.1	3.7 ± 0.3	2.6 ± 0.5	28.3 ± 0.6

r_x, r_y, and r_z denote rotational angles (degrees) about X, Y, and Z-axes, respectively. t_x, t_y, and t_z denote translations (mm) along X, Y, and Z axes, respectively

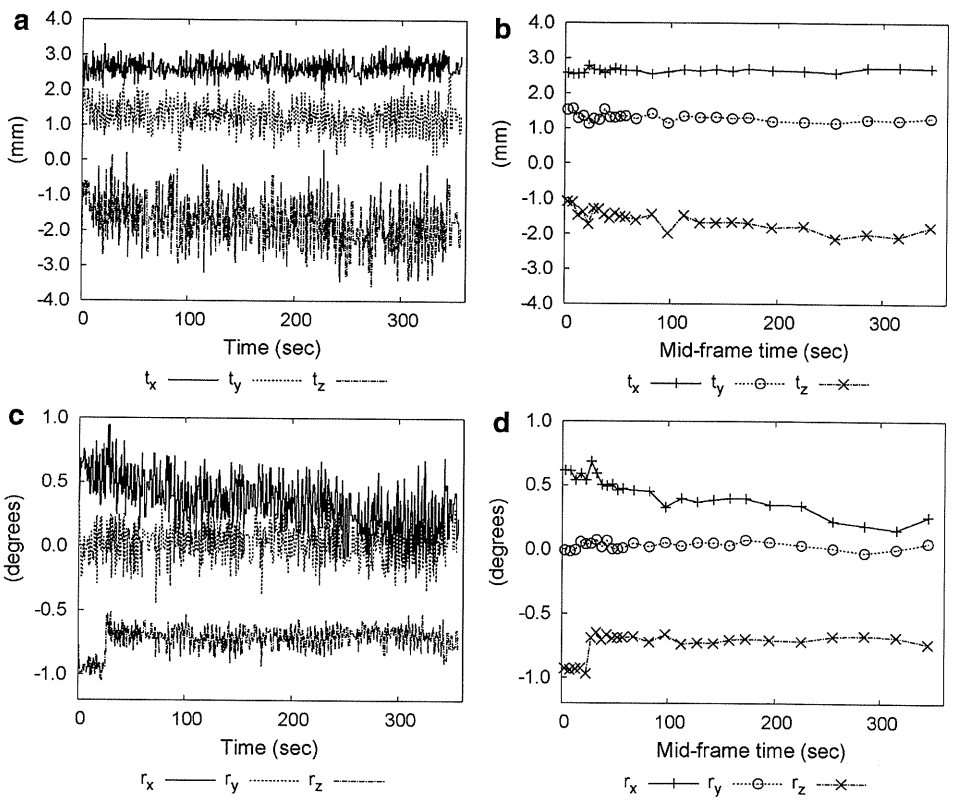

Fig. 4 Motion parameters during ^{15}O-water study on the healthy volunteer. **a**, **b** Sample-by-sample and frame-averaged translations. **c**, **d** Sample-by-sample and frame-averaged rotational angles

Table 4 MBF values (mL/min/g of perfusable tissue) of the healthy volunteer

Myocardial region	Case			
	1	2	3	4
Apical	1.05	1.00	0.99	1.05
Mid-anterior	0.92	0.89	1.26	0.99
Mid-lateral	0.93	0.89	1.38	0.89
Mid-posterior	1.14	1.16	0.96	1.01
Mid-septal	1.05	1.06	1.08	1.12
Basal-anterior	0.87	0.80	1.18	0.80
Basal-lateral	0.86	0.82	0.95	0.84
Basal-posterior	0.88	0.83	0.84	0.86
Basal-septal	0.73	0.72	0.65	0.82
Mean ± SD	0.94 ± 0.12	0.91 ± 0.13	1.03 ± 0.21	0.93 ± 0.11

differences in the mid-anterior and mid-lateral regions as well as the basal-anterior regions between cases 1 and 3.

Figure 5 demonstrates the influence of misalignment between an attenuation map and emission data on the quality of myocardial images, as well as the effect of our correction technique. Figure 5a–f represent the build-up and washout phase images of middle myocardial obtained from the ^{15}O-water data. Anterior, lateral, posterior, and septal regions of myocardia were arranged in a clockwise manner. Figure 5a and e was obtained from the data of case 1, and Fig. 5b and f was calculated from the data obtained in case 2. Figure 5c and g was derived from the data in case 3, and only positions of reconstructed images were transformed to the first transmission coordinate after reconstructions for visual

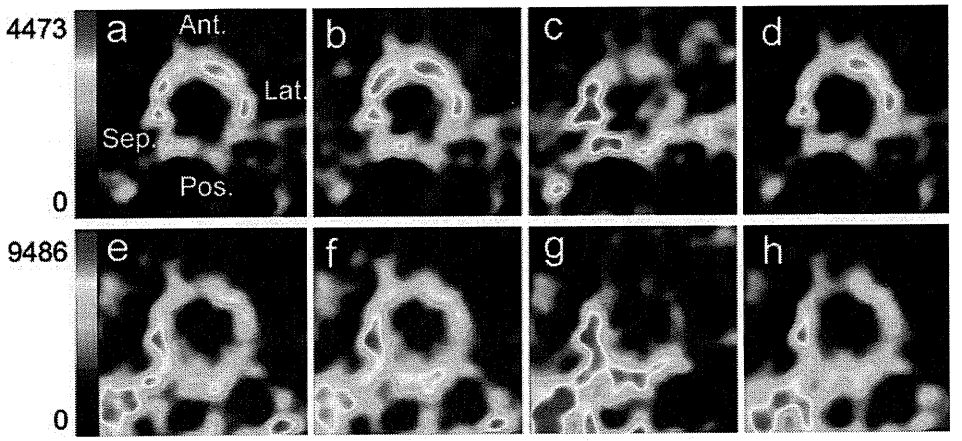

Fig. 5 Myocardial images of the healthy volunteer. **a–d** Build-up phase images. **e–h** Washout phase images. **a** and **e** were reference images obtained from data of case 1. **b** and **f** are images from data of case 2, which were corrected for the motions of the subject. **c** and **g** are images from case 3 of the emission data and the second attenuation map without our motion corrections. **d** and **h** are images from case 4, which were corrected for the motions and the misalignment between the emission data and the second attenuation map

comparison with the other images. Figure 5c and g demonstrates that reconstruction with an incorrect attenuation map caused spurious defects from anterior to lateral myocardial regions, as well as an artifact in the posterior region. Figure 5d and h is an image calculated from data obtained in case 4, in which images were also transformed to the first transmission coordinate.

Discussion

In this paper, we developed an optical motion-tracking based system to detect global movement of the subject and correct for the movement during cardiac ^{15}O-water studies.

First, the inherent accuracy of the system was assessed from position calibrations. As shown in Table 1, the $T_{G\rightarrow S}$ part could be negligibly small compared with the magnitude of the subject's motions in Table 3 and Fig. 4. For the $T_{S\rightarrow P}$ part shown in Table 1, there was no bias in any direction. The value of RMSE for each scanner was smaller than the spatial resolution of the scanner [21, 22]. Therefore, it was considered that the position calibrations provided a sufficient level of accuracy for our motion corrections.

To validate the present technique, we performed a cardiac phantom study. As shown in Fig. 3a, a defect and blurred region from the anterior to the lateral, which was mainly caused by a 5.1° rotation about the Z axis and a 35.7 mm shift along the X axis, was recovered using the present technique. The effect of the present technique was also shown more objectively by the correlation coefficients and profile comparison in Fig. 3b.

In the healthy volunteer study, no correction was applied for the motions of the subjects during the transmission scans because the PET scanners do not have the ability to perform dynamic transmission scans. Motions during a transmission scan resulted in a blurred attenuation map, and caused over- or under-estimation of the radioactive concentration in myocardium of ^{15}O-water images. However, as shown in Table 3, the magnitudes of the mean and SD during the transmission scans were smaller than the spatial resolution provided by the PET scanner, even if the magnitudes were slightly larger than those of the mean and SD during emission scans. In addition, a 9-mm smoothing filter was employed during the image reconstruction stage. Therefore, we considered that valid transmission data were acquired for the subject. For the same reason as in the case of the transmission data, the emission data of ^{15}O-water scan were acquired properly. So we used the data of case 1 as the reference for the other cases.

The global movement and cyclic movement of the target were observed as shown in Fig. 4a and c. The cyclic movement was attributed to respiration. From Fig. 4b and d, the cyclic movement was smoothed by frame-averaging. In addition, the regional MBF values (Table 4) and the myocardial images (Fig. 5) of cases 1 and 2, which were derived from the same transmission and emission scans before and after the motion correction, were nearly the same. This result indicated that our system provided reasonably accurate information about the global movement.

In case 3, in which no correction for the subject's motions and the 30-mm shift between the emission data and the second attenuation map was applied, the MBF values for the mid-anterior, mid-lateral, and basal-anterior regions were

significantly larger than the reference values. This overestimation was associated with spurious defects from the anterior to lateral regions, as shown in Fig. 5c and g. In case 4 with our correction technique, the MBF values for myocardial regions, in which overestimated MBFs were obtained for the corresponding regions in case 3, were similar to the reference values. The image quality in Fig. 5d and h was also nearly the same as in Fig. 5a and e. Figure 5d shows a clearly delineated contour of the myocardial region similar to the contour in Fig. 5a. The spurious defects from the anterior to lateral regions in Fig. 5g were recovered in Fig 5h. Owing to these results, the present technique tracked the location of the external target attached to the chest skin accurately, and then corrected the artificial misalignment during transmission and emission scans. Figure 5 not only shows the effects of our correction technique, but also suggests that the use of an attenuation map with large global movement could cause the appearance of spurious defects in myocardial imaging with ^{15}O-water PET.

Several listmode-based motion correction techniques have hitherto been proposed [1, 3–7]. Compared to these techniques, our technique provides poorer time resolution, even though our technique was applied to an emission scan consisting of dynamic frames with shorter duration. Listmode-based methods, however, require wide band transmission and high computational power for manipulating the listmode event data, especially under high count rates. For the listmode-based methods, in which data processing is conducted prior to the motion correction, corrections for detector efficiency, detector geometry, and crystal interferences are important issues, especially in the case of scanners with gaps between detectors or no intersection of motion-corrected LOR with detector(s). For our technique with 2D acquisition mode, the sinogram data are simply normalized by the built-in software of the used PET scanners. Our technique could shorten the processing time by re-binning the listmode data during the period when substantial movement is detected, and then correcting the re-framed dynamic sinogram. Furthermore, our technique is applicable to many commercially available PET scanners, which often have no feasibility of listmode acquisition.

Instead fixating the POLARIS on a certain position, such as the gantry of the PET scanner described in [3, 6], we attached the reference target onto the gantry and then used the target and the calibration tool to transform the subject's position from the POLARIS coordinate to the PET coordinate. Thus, our method allows for more flexibility in adjusting with regard to the location of the POLARIS. This is an important feature for the cardiac study due to the large inter-subject variability in the shapes of the torsos among patients, and as shown in Fig. 1e, there were enough gaps to set the best positioning for cardiac PET study. However, for exercise study, such as the studies with cycling, smaller targets and supporting post might be needed to ensure working space. An additional advantage is the portability of the POLARIS, which enables the sharing of the device among scanners in different locations.

For our technique based on the rigid body model, two targets were enough to detect the displacements and rotations of the thoraxes of the subjects, in which the secondary target was used as a reserve for cases in which the primary target was hidden from the FOV of the POLARIS. The secondary target and additional targets might be used with the corporation of the primary target to construct a non-rigid body model by detecting deformation between the chest and abdomen, and/or over the thorax region.

Another approach for the motion correction was based on image-driven information. Juslin et al. proposed an alignment technique for dynamic ^{15}O-water PET images by means of the independent component analysis. They demonstrated an improvement in quantitatively functional and parametric values, although they did not take into account for the misregistration between the transmission and emission data sets, and the movements during each emission scan [24]. The advantages of our method comparing software-based technique were (1) the misalignment between the transmission and dynamic image, and misalignment among the dynamic images could be corrected because our method was independent of the distribution and concentration of the tracer, and suboptimal image qualities (e.g., statistical noise, blurring and types of tracers). (2) Accurate attenuation correction was available because the misalignment between the transmission and the dynamic image was corrected in the reconstruction stage of the dynamic image, and (3) inherent accuracy could be obtained from the position calibration and the optical motion tracking device. Consequently, the present technique can be utilized in PET studies with several types of tracers such as ^{13}N-Ammonia and ^{18}F-FDG.

In this study, the motion correction system was demonstrated on one subject at rest. The system is to be evaluated by large population of various subjects because characteristics of motion such as magnitudes, frequencies, and directions could be different among subjects. Validation of our system is also needed for the studies during the physiologically or pharmacologically stressed conditions, in which repositioning of the heart in thoracic cavity, and larger and/or irregular (non-cyclic) chest motion by respiration would be expected. In our method, one of the limitations was correction for the misalignment due to the motion of the diaphragm with a deep breathing during a stress study, and due to the motion of the diaphragm with cough or sneezing even though during a resting study. To correct such misalignment, detection of irregular motion and a non-linear model might be needed to estimate the

location of the heart using information obtained from the locations of targets on the chest.

Our system intended to correct global movement during dynamic scans. It was expected that the system would work on transmission and emission data smoothed temporally and spatially. Attenuation correction artefacts due to respiration was out of the scope for our system, which were investigated in the X-ray combined PET system studies [25, 26].

Conclusion

Our technique using an optical motion-tracking device provided the reasonable information for correcting the global movement of the subject. It was shown that this system was applicable to detect and correct subject movement in cardiac PET studies at rest. We conclude that the present technique would contribute to improvement in the quantification of MBF in ^{15}O-water PET studies.

Acknowledgments This study was supported by a grant from New Energy and Industrial Technology Development Organization (NEDO) of Japan, the Budget for Nuclear Research of the Ministry of Education, Culture, Sports, Science and Technology (MEXT) of Japan, the Program for Promotion of Fundamental Studies in Health Science of the Organization for Pharmaceutical Safety and Research of Japan, Health Science Research Grant from the Ministry of Health, Labour and Welfare of Japan, a Grant-in-Aid for Young Scientists of the MEXT (B) (19700397) of Japan, and also a research grant for Advanced Medical Technology from the Ministry of Health, Labour and Welfare (MHLW) of Japan.

References

1. Menke M, Atkins MS, Buckley KR. Compensation methods for head motion detected during PET imaging. IEEE Trans Nucl Sci. 1996;43:310–7.
2. Picard Y, Thompson CJ. Motion correction of PET images using multiple acquisition frames. IEEE Trans Med Imaging. 1997;16:137–44.
3. Lopresti BJ, Russo A, Jones WF, Fisher T, Crouch D, Altenburger DE, et al. Implementation and performance of an optical motion tracking system for high resolution brain PET imaging. IEEE Trans Nucl Sci. 1999;46:2059–67.
4. Watabe H, Sato N, Kondoh Y, Fulton RR, Iida H. Correction of head movement using optical motion tracking system during PET study with rhesus monkey. In: Brain Imaging Using PET. San Diego: Academic Press; 2002. p. 1–8.
5. Fulton RR, Meikle SR, Eberl S, Pfeiffer J, Constable CJ. Correction for head movements in positron emission tomography using an optical motion-tracking system. IEEE Trans Nucl Sci. 2002;49:116–23.
6. Bloomfield PM, Spinks TJ, Reed J, Schnorr L, Westrip AM, Livieratos L, et al. The design and implementation of a motion correction scheme for neurological PET. Phys Med Biol. 2003;48:959–78.
7. Woo SK, Watabe H, Yong C, Kim KM, Choon C, Bloomfield PM, et al. Sinogram-based motion correction of PET images using optical motion tracking system and list-mode data acquisition. IEEE Trans Nucl Sci. 2004;51:782–8.
8. McCord ME, Bacharach SL, Bonow RO, Dilsizian V, Cuocolo A, Freedman N. Misalignment between PET transmission and emission scans: its effect on myocardial imaging. J Nucl Med. 1992;33:1209–14.
9. Germano G, Chua T, Kavanagh PB, Kiat H, Berman DS. Detection and correction of patient motion in dynamic and static myocardial SPECT using a multi-detector camera. J Nucl Med. 1993;34:1349–55.
10. Cooper JA, Neumann PH, McCandless BK. Detection of patient motion during tomographic myocardial perfusion imaging. J Nucl Med. 1993;34:1341–8.
11. Bacharach SL, Douglas MA, Carson RE, Kalkowski PJ, Freedman NM, Perrone-Filardi P, et al. Three-dimensional registration of cardiac positron emission tomography attenuation scans. J Nucl Med. 1993;34:311–21.
12. Iida H, Kanno I, Takahashi A, Miura S, Murakami M, Takahashi K, et al. Measurement of absolute myocardial blood flow with $H_2^{15}O$ and dynamic positron-emission tomography. Strategy for quantification in relation to the partial-volume effect. Circulation 1988;78:104–15 (erratum in: Circulation 1988;78:1078).
13. Iida H, Rhodes CG, de Silva R, Yamamoto Y, Araujo LI, Maseri A, et al. Myocardial tissue fraction–correction for partial volume effects and measure of tissue viability. J Nucl Med. 1991;32:2169–75.
14. Knaapen P, Boellaard R, Götte MJ, van der Weerdt AP, Visser CA, Lammertsma AA, et al. The perfusable tissue index: a marker of myocardial viability. J Nucl Cardiol. 2003;10:684–91.
15. de Silva R, Yamamoto Y, Rhodes CG, Iida H, Nihoyannopoulos P, Davies GJ, et al. Preoperative prediction of the outcome of coronary revascularization using positron emission tomography. Circulation. 1992;86:1738–42.
16. Knaapen P, Boellaard R, Götte MJ, Dijkmans PA, van Campen LM, de Cock CC, et al. Perfusable tissue index as a potential marker of fibrosis in patients with idiopathic dilated cardiomyopathy. J Nucl Med. 2004;45:1299–304.
17. Chareonthaitawee P, Kaufmann PA, Rimoldi O, Camici PG. Heterogeneity of resting and hyperemic myocardial blood flow in healthy humans. Cardiovasc Res. 2001;50:151–61.
18. Yamamoto Y, de Silva R, Rhodes CG, Araujo LI, Iida H, Rechavia E, et al. A new strategy for the assessment of viable myocardium and regional myocardial blood flow using 15O-water and dynamic positron emission tomography. Circulation. 1992;86:167–78.
19. Iida H, Rhodes CG, de Silva R, Araujo LI, Bloomfield PM, Lammertsma AA, et al. Use of the left ventricular time-activity curve as a noninvasive input function in dynamic oxygen-15-water positron emission tomography. J Nucl Med. 1992;33:1669–77.
20. Naum A, Laaksonen MS, Tuunanen H, Oikonen V, Teräs M, Kemppainen J, et al. Motion detection and correction for dynamic (15)O-water myocardial perfusion PET studies. Eur J Nucl Med Mol Imaging. 2005;32:1378–83.
21. Iida H, Miura S, Kanno I, Ogawa T, Uemura K. A new PET camera for noninvasive quantitation of physiological functional parametric images: HEADTOME-V-Dual. In: Quantification of brain function using PET. San Diego: Academic Press; 1996. 57–61.
22. Wienhard K, Dahlbom M, Eriksson L, Michel C, Bruckbauer T, Pietrzyk U, et al. The ECAT EXACT HR: performance of a new high resolution positron scanner. J Comput Assist Tomogr. 1994;18:110–8.

23. Iida H, Rhodes CG, Araujo LI, Yamamoto Y, de Silva R, Maseri A, et al. Noninvasive quantification of regional myocardial metabolic rate for oxygen by use of $^{15}O_2$ inhalation and positron emission tomography. Theory, error analysis, and application in humans. Circulation. 1996;94:792–807.
24. Juslin A, Lötjönen J, Nesterov SV, Kalliokoski K, Knuuti J, Ruotsalainen U. Alignment of 3-dimensional cardiac structures in O-15-labeled water PET emission images with mutual information. J Nucl Cardiol. 2007;1:82–91.
25. McQuaid SJ, Hutton BF. Sources of attenuation-correction artefacts in cardiac PET/CT and SPECT/CT. Eur J Nucl Med Mol Imaging. 2008;35:1117–23.
26. Gould KL, Pan T, Loghin C, Johnson NP, Guha A, Sdringola S. Frequent diagnostic errors in cardiac PET/CT due to misregistration of CT attenuation and emission PET images: a definitive analysis of causes, consequences, and corrections. J Nucl Med. 2007;48:1112–21.

特集

ここまできた神経画像

核医学的測定法の進歩

飯田秀博，銭谷 勉，越野一博，平野祥之
IIDA Hidehiro, ZENIYA Tsutomu, KOSHINO Kazuhiro, HIRANO Yoshiyuki
国立循環器病センター研究所・先進医工学センター　放射線医学部

PET 装置は検出器の精細化で空間解像度の上昇が進み，立体撮像によって高感度化が実現した．SPECT においては吸収と散乱線を正確に補正する画像再構成プログラムの利用によって，定量化と標準化が可能になった．このようななかで，従来よりも一歩踏み込んだ脳神経核医学画像の定量評価が可能になる．複数モダリティイメージングに加えて，調節機能などの診断は今後の課題である．

Key Words
機能画像，マルチモダリティ，マルチトレーサ，時間解像度

はじめに

PET が誕生してから 30 年以上の技術蓄積の結果，検出器の改良は空間解像度の一桁向上に，多断層化と立体計測技術の普及は感度の二桁上昇に貢献した．SPECT においては複数検出器やコリメータの進歩，さらに画像再構成理論の改善によって定量精度改善がなされた．複数モダリティの融合画像処理技術や，新しい画像再構成理論の整備と実用化も進み，神経画像の高精細化に貢献する．本稿では，新しい要素技術とその効果について概説する．

1　PET

PET 装置の空間解像度を決定するのはシンチレーション結晶の大きさであり，小型ブロック検出器の開発が高解像度化に貢献してきた．深さ情報（depth-of-interaction：DOI）を検出する検出器も実用化された．立体計測（三次元，3D）は完全に定着し測定感度は大きく改善し，1%を超えるに至った．臨床 PET 装置の空間解像度は概ね 4 mm 程度にまで向上した．画像再構成プログラムはさらに改良が進み，吸収補正や散乱線補正に加えて空間解像度の補正がなされるようになり，空間解像度は 2 mm 程度になったとされる．高性能な放射線検出シンチレータの実用化がなされ，また同時計測の時間分解能（coincidence window）が短くなった．これは画質劣化の最大の要因であった偶発同時計数の減少に貢献する．一部のメーカーでは time-of-flight 処理（同時計測信号の時間差より線源の場所を限局する機構）も搭載される．

現在の課題は，膨大な情報の高速処理技術の開発にあるといえる．PET では検出器総数の自乗に比例した計測線（line-of-response：LOR）の信号を扱う．典型的には

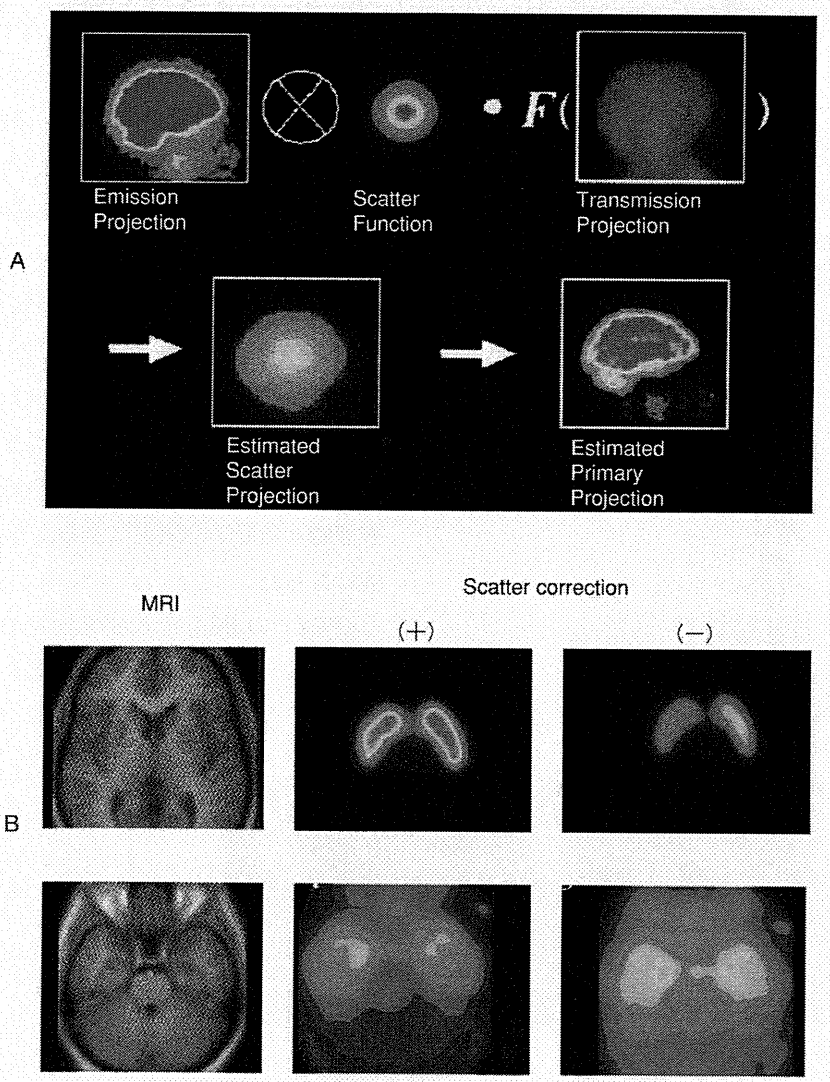

図❶ 定量的 SPECT 画像再構成における散乱線補正の効果
(A：Iida H *et al*, 1998[2], B：Fujita M *et al*, 2004[4]より引用)
A：散乱線補正法の例．吸収減弱プロジェクションを利用した方法はノイズの高揚がなく良好な画像を提示する．B：I-123 標識 epidepride の結合能画像における散乱線補正の効果．散乱線補正は画像のコントラストを上昇させ，定量解析には不可欠である．

10^8にもなる LOR 信号を演算処理・保存するためには相当高速な電子回路を含む処理技術が必要である．また，3D PET 計測における散乱線を補正する普遍的な方法も確立されなければいけない．放射線分布と吸収減弱 (μ) 分布に物理公式 (Klein-Nishina の式など) を適用する方法が提案されているが，視野外の放射能や散乱線発生の影響は意外に少ないことが当該研究グループ平野らによって明らかにされ，この方法の妥当性，また視野シールドの有効性が確認されたところである．いずれにせよ神経イメージングに向けた PET 計測技術は着実に進んでおり，さらに明瞭かつ高精度な画像の撮像が可能になる．

2 SPECT

SPECT 技術の最近の重要な進展は，定量化と標準化に向けた活動であろう．SPECT 画像の定量精度の確保は困難とされてきたが，吸収と散乱線を比較的正確に補正する実用的なプログラムの整備によって，メーカーや機種を超えた再現性が得られるようになった．これは施設を

超えてデータが共有できる点においても，また既存の装置がそのまま利用できる点においても，PET に勝る重要な特長である．SPECT を使った多施設臨床研究は困難とされてきたが[1]，当該研究者らが中心となっておこなった施設を超えた画像の蓄積や大規模臨床研究において，集約解析の妥当性が支持された．また SPECT の定量精度の向上によって，高度な動態解析（コンパートメントモデル解析）が可能になったことも重要である．とくに散乱線は画像のコントラストを低下させていたが，**図❶A**[2]にみるようにこれがよく改善されたことで，脳神経受容体の結合能の定量評価[3)~5)]（**図❶B**）や，一回の撮像で安静時と負荷時の測定による血管反応性の診断などが可能になった．

SPECT の PET とくらべた最大の欠点は感度が低いことである（PET とくらべておよそ 10^{-3}）．放射線計測の

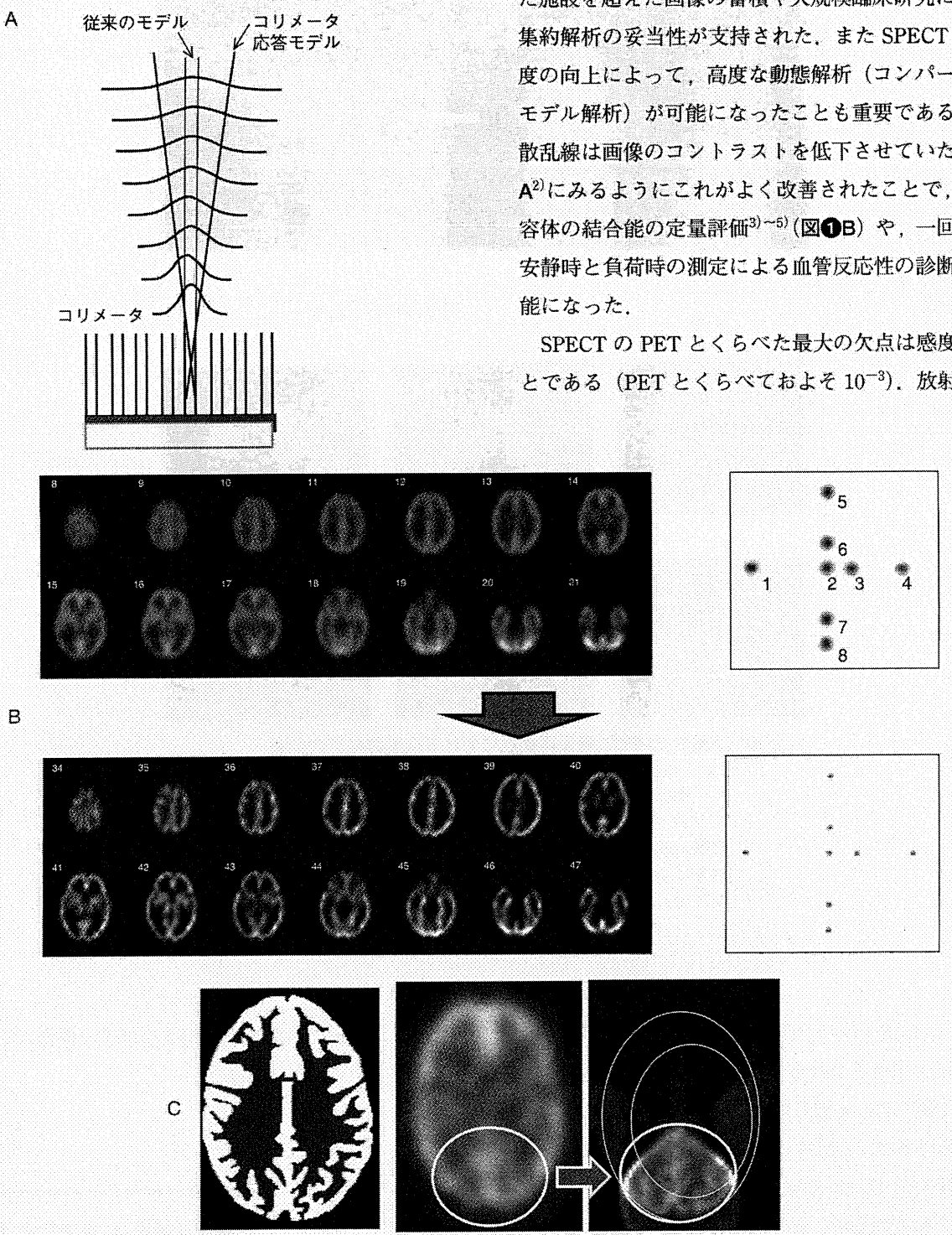

図❷ SPECT 画像再構成における空間解像度の補正
A：コリメータ開口にもとづく空間解像度劣化のモデル．B：コリメータ開口の補正を組み込むことで，空間解像度は 9.0 mm から 5.0 mm 以下に改善し，また統計ノイズも軽減された．今後臨床診断での実用化が望まれる．C：局所領域にピンホールコリメータの焦点を設定して得た 3D Hoffman ファントムの Tc-99m 画像．従来の画像撮像よりも局所において空間解像度の上昇が確認される．

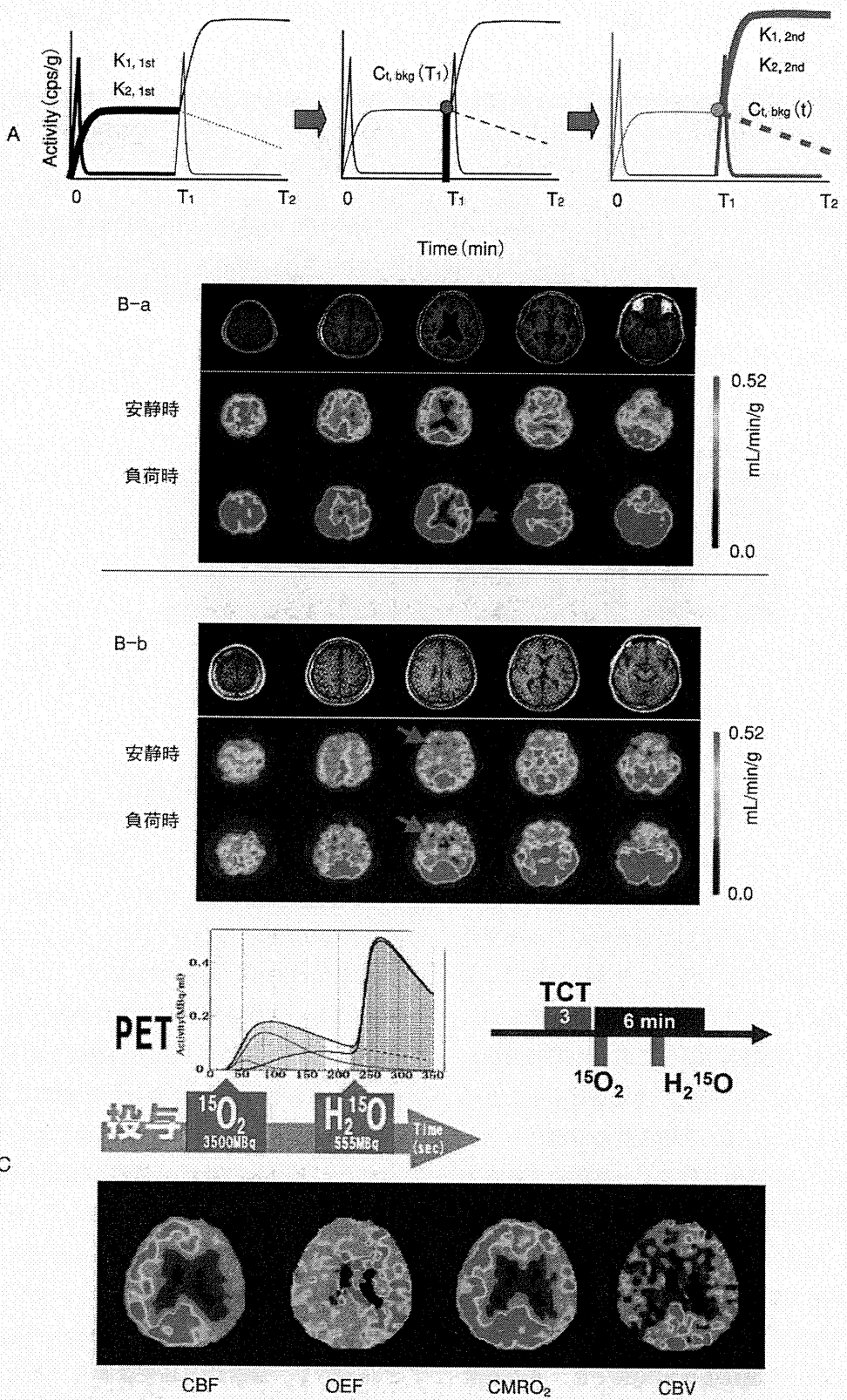

図❸ 複数薬剤投与法の効果

A：複数トレーサ投与時の入力関数と脳内放射能濃度曲線を示す．バックグランド画像を推定し，さらに2回目投与後の脳内放射能濃度から機能画像を推定することが可能である．B：I-123 IMP の2回連続投与法にもとづく典型的な安静時とダイアモックス負荷後の局所脳血流量画像．症例 a では軽度血管狭窄を予測し，症例 b では高リスク血管狭窄を予測した．C：迅速^{15}O-ガス PET 検査への利用．従来1時間以上を要していた一連の検査が，10分間以内のスキャンで可能になった．